Ultra-stable all-solid-state sodium-metal batteries enabled by perfluoropolyether-based electrolytes

Xiaoen WANG
Deakin University https://orcid.org/0000-0001-7713-7062
Cheng Zhang
The University of Queensland
Michal Sawczyk
University of Illinois at Chicago https://orcid.org/0000-0002-0827-4036
Qinghong Yuan
The University of Queensland
Fangfang Chen
Deakin University
Tiago Mendes
Deakin University
Patrick Howlett
Deakin University https://orcid.org/0000-0002-2151-2932
Changkui Fu
The University of Queensland
Debra J. Searles
University of Queensland https://orcid.org/0000-0003-1346-8318
Petr Kral
University of Illinois at Chicago https://orcid.org/0000-0003-2992-9027
Craig Hawker
UC - Santa Barbara https://orcid.org/0000-0001-9951-851X
Andrew Whittaker
The University of Queensland
Maria Forsyth (maria.forsyth@deakin.edu.au)
Deakin University https://orcid.org/0000-0002-4273-8105

Article

Keywords: rechargeable batteries, solid polymer electrolytes, polyethylene glycol

Posted Date: April 2nd, 2021

DOI: https://doi.org/10.21203/rs.3.rs-354912/v2

Version of Record: A version of this preprint was published at Nature Materials on July 4th, 2022. See the published version at https://doi.org/10.1038/s41563-022-01296-0.

Abstract

Rechargeable batteries paired with sodium (Na)-metal anodes are considered as one of the most promising high energy and low-cost energy storage systems. However, the use of highly reactive Na metal and the formation of Na dendrites during battery operation have caused significant safety concerns, especially when highly flammable liquid electrolytes are used. Herein, we design and develop a solvent-free solid polymer electrolytes (SPEs) based on a perfluoropolyether (PFPE) terminated polyethylene glycol (PEG)-based block copolymer for safe and stable all-solid-state Na-metal batteries. Compared with traditional poly(ethylene oxide) (PEO) or PEG SPEs, our results suggest that block copolymer design allows for the formation of self-assembled microstructures leading to high storage modulus at elevated temperatures with the PEG domains providing transport channels even at high salt concentration (EO/Na^+ = 8:2). Moreover, it is demonstrated that the incorporation of PFPE segments enhances the Na^+ transference number of the electrolyte to 0.46 at 80 ^oC. Finally, the proposed SPE exhibits highly stable symmetric cell cycling performance with high current density (0.5 mA cm^{-2} and 1.0 mAh cm^{-2}, up to 1300 hours). The assembled all-solid-state Na-metal batteries with $Na_3V_2(PO_4)_3$ cathode demonstrate outstanding rate performance, high capacity retention and long-term charge/discharge stability (CE = 99.91%) after more than 900 cycles.

Introduction

Sodium (Na) ion batteries are recognized as attractive energy storage devices for next generation large-scale applications due to the high abundance and wide distribution of Na resources.[1, 2] In addition, benefiting from its high theoretical specific capacity (1165 mAh g^{-1}) and low redox potential (-2.714 V *vs* standard hydrogen electrode), the use of Na metal as anodes further boosts the overall battery capacity, enabling the next generation of low-cost, high-capacity batteries.[3–5] However, the development of Na-metal batteries faces significant challenges.[6, 7] For instance, the extensive use of highly flammable liquid carbonate electrolytes can lead to catastrophic hazards such as fire and explosions. Furthermore, these organic solvent based electrolytes do not support stable long term cycling of Na metal.

In contrast, the development of all solid-state Na-metal batteries with the absence of any flammable liquid shows significant advantages for improving battery safety. Several strategies have been intensively investigated including solid-state inorganic Na^+ conductors such as sulfides (Na_3PS_4), NASICON and β-alumina.[8] Although these inorganic conductors show remarkable conductivity at room temperature and suitable electrochemical stability,[9] the physical point-to-point contacts at the electrolyte/electrode interface are problematic as these insufficient contacts will dramatically increase interfacial resistance, leading to poor cycling stability and final battery failure.[10] In addition, the ability of inorganic systems to suppress dendrite formation remains a continuing topic of debate as some recent work illustrates metallic dendrite growing through the inorganic electrolytes via material defects such as voids or cracks.[10]

As an alternative to rigid inorganic electrolytes, solvent-free polymer electrolytes are attractive due to their flexibility, suitable mechanical strength and high electrochemical stability.[11–16] The traditional polymer electrolytes consist of a host polymer such as poly(ethylene oxide) (PEO) and Na salts. PEO-based solid polymer electrolytes (SPEs) show good Na salt solubility due to the coordination between ether oxygen and Na^+, however, this interaction is relatively strong, which limits the Na^+ movements. As a result, low transference numbers (t_{Na+}), defined as the ratio of current carried by Na^+ to the total current carried by all mobile charges,[17] are obtained. Furthermore, due to the high reactivity of Na metal, poor interfacial stability between PEO electrolytes and the Na anode is another hindrance for achieving long life-time battery performance. Previous studies have also demonstrated that the side reactions between the electrolyte and Na metal will result in an increase in interfacial resistance and subsequent battery failure during long-term cycling. With the aim of improving Na metal stability during operation, Hu and co-workers recently proposed an effective strategy to take advantage of NaFSI hydrolysis combined with Al_2O_3 nanoparticles.[18] They confirmed that the side product of this composite electrolyte can effectively form a protective layer, leading to enhanced columbic efficiency and stable long term charge/discharge performance at 80 ^oC. In addition, the emergence of fluorinated electrolytes provides an effective method to stabilize metal anodes and improve cycling stability. Wang *et al.* demonstrated that a thin LiF-rich solid-electrolyte-interphase (SEI) layer can be formed when fluorinated liquid electrolytes are used.[19] The advantages of fluorinated electrolytes were further confirmed through design of fluorinated ether electrolytes which enable long term cycling of Li-metal batteries.[20–22] Moreover, Balsara and co-workers demonstrated that the interactions between fluorinated segments and salt anions can effectively enhance the Li^+ transference number and Li^+ conductivity.[23] Unfortunately, all of these previous reports focused on the design of fluorinated liquid electrolytes and their applications in lithium batteries.[24] Examination of SPEs with fluorinated components and their applications on Na-metal batteries are yet to be investigated.

In this work, for the first time, a new class of fluorinated block copolymer is designed as a solid electrolyte for the development of highly stable, all-solid-state Na-metal batteries. We demonstrate that the introduction of perfluoropolyether (PFPE) domains into PEG-based electrolytes can effectively enhance the mechanical properties of polymer electrolytes due to the formation of self-assembled microstructures. Compared with traditional non-fluorinated PEG electrolytes, these new PFPE-based SPEs significantly improve Na^+ transport and increase the Na^+ transference number. More importantly, the presence of PFPE segments in the polymer electrolyte leads to outstanding cycling stability (1000 h) at 1.0 mAh cm^{-2} plating/striping capacity with Na metal anode. Finally, all-solid-state Na-metal batteries based on fluorinated SPE composites show promising rate capability and long-term stability, allowing over 900 cycles with an average coulombic efficiency of 99.91% at 80 ^oC. The study promises opportunities for the design of new fluorinated copolymers as highly stable solid polymer electrolytes for Na-based battery applications

Results And Discussion

Rational Design, Structure and Thermal Properties of PFPE Electrolytes

We have designed and investigated a new class of fluorinated block copolymer with controlled morphology as a SPE to enhance mechanical integrity, interfacial stability and Na^+ transport. The copolymer consists of a PFPE-based segment as the fluorinated block and oligo(ethylene glycol) methyl ether acrylate (PEGA) as the soft block (poly(PEGA)m-PFPE or EOm-PFPE, where m is the degree of polymerization (*DP*) of PEGA). The synthetic details and characterization data for the copolymers are shown in the experimental section and Table S1.[25–34] Fig. 1a illustrates the chemical structures of PFPE polymer (EO10-PFPE) and control polymer (EO10-CTRL). In this strategy, the dissociated Na^+ ions in the PEG domain undergo efficient transport with the assistance of ether oxygen side chain relaxation, while the phase separation between the PEG and PFPE blocks maintains the mechanical integrity. The fluorinated segments are also designed to stabilize the alkali metal anode, Na metal in this study, through the potential for formation of stable fluorinated compounds in the SEI layer.[35]

The interactions between polymers and alkali metal ions play a crucial role in the determination of polymer electrolyte properties and thus the battery performance. Previous reports have shown that the strength of coordination between the ether oxygen groups of the PEG backbone and alkali metal ions significantly affect the physical properties of the resultant polymer electrolytes.[36] The investigation of thermal behavior *i.e.* glass transition temperature (T_g) can ultimately help to understand such interactions in different electrolyte systems. For example, differential scanning calorimetry (DSC) measurements of neat EO10-PFPE copolymers show a glass transition temperature (T_g) at -59.3 ^oC and an endothermic melting peak (T_m) located between − 20 to 20 ^oC (Figure S1, S2), associated with the glass-to-rubber relaxation and melting of the PEG domains, respectively. The glass transition and melt characteristics are well maintained in all PFPE-containing block polymers with different *DP*s of PEGA. Significantly, after adding NaFSI salt, the melting peak of PFPE polymers completely disappears (Figure S1). Another notable change is that, due to the strong coordination between ether oxygen and Na^+ ions, the addition of NaFSI increases the T_g of the PEG segments dramatically from ≈ − 60 to above − 40 ^oC for all four of the EOm-PFPE copolymers (m = 5, 10, 20, 40) (Figure S2). A further investigation shows that the T_g of these copolymer electrolytes highly depends on the salt concentration. As displayed in Fig. 1b, Figure S3 and Table S2, increasing the NaFSI concentration lifts T_g continuously from − 59.3 to − 6.8 ^oC when the EO/Na ratio increases from 8/0 to 8/4 for the EOm-PFPE electrolyte. The shift in T_g to higher temperatures indicates enhanced conformational constraints of the PEG segment relaxation processes at high concentration of salts, leading to reduced polymer flexibility and increased T_g.[36] In addition, a relatively small T_g increase rate in the high salt content region is observed (8/2 to 8/4, Fig. 1b), indicating the approach to a maximum coordination of ions in the PEG domains.[37]

Another important observation is that the introduction of the PFPE blocks enhances the relaxation of the PEG domain due to the formation of self-assembled structures. Compared with EO10-CTRL electrolyte,

the EO10-PFPE with same EO/Na^+ ratio shows a lower T_g (Fig. 1b, Figures S3-S4 and Table S2) when NaFSI is added. We ascribe the relatively lower T_g to confinement effects on the dynamics of the EO-Na^+ complex, which is in good agreement with previously reported hybrid electrolyte systems.[38, 39] As shown in Fig. 1c, the introduction of the PFPE block into PEG leads to the formation of self-assembled body-centered cubic (BCC) microstructures. The presence of confinement in the microstructures allows the physical properties of polymer electrolyte materials such as T_g, mobile diffusivity and molecular packing density to be modulated.[40–43] For instance, a larger free volume and separated phase with enhanced dynamics are suggested in confined silica nano pores.[38, 44] Similarly, when NaFSI is added into EO10-PFPE, the EO-Na^+ complex will be mainly located in the PEG domains, therefore the confinement effects in self-assembled structures will provide more free volume, resulting in a lower T_g.[38] Meanwhile the self-assembled BCC structures of EO10-PFPE electrolyte are maintained at higher temperatures with an order-disorder transition temperature (T_{ODT}) at 100°C, as determined by dynamic mechanical thermal analysis (DMTA, Figure S4). Figure 1d shows the frequency sweep storage (G') and loss modulus (G'') of EO10-PFPE electrolytes at 80 °C. G' is distinctly greater than G'' in the full frequency window (10^{-2} – 10^2 Hz), implying a solid-like behavior of the EO10-PFPE electrolyte even at 80 °C. In addition, the storage modulus G' is closer to the loss modulus G'' at lower frequencies, indicating the soft behavior of the electrolyte, potentially allowing the PFPE electrolyte to adapt and achieve good contact with the electrodes, even with the unpredictable volume changes that may occur during cycling.[45] This mechanical integrity at elevated temperatures is highly desirable for all solid battery devices and applications.[46]

Ionic Conductivity, Molecular Interaction and Electrochemical Properties

Based on the SAXS results in Fig. 1c, the microstructures of EO10-CTRL and EO10-PFPE electrolytes are illustrated in Fig. 2a. Compared with the liquid-like EO10-CTRL electrolyte (Figure S6), the introduction of the PFPE block leads to the formation of a solid-state material with phase-separated microstructure (PFPE-rich and PEG-NaFSI-rich domains).[47, 48] Further incorporation of poly(vinylidene fluoride) (PVDF) electrospun fibers (scanning electron microscope (SEM) image shown later in Fig. 4a) results in a free-standing electrolyte membrane with thickness around 100 μm (inset in Fig. 2b). Furthermore, the SEM images in Fig. 2b and 2c confirm the pores of the PVDF matrix are completely filled with EO10-PFPE electrolyte, leading to a flexible solvent-free SPE that is highly desirable for solid-state battery devices. By contrast, the EO10-CTRL composite is a soft and non-free-standing membrane which deforms easily, even in the absence of external force (Figure S6).

As shown in Fig. 2d, the conductivity of EO10-PFPE SPE is increased when compared to that of the parent EO10-CTRL electrolyte over the whole temperature range, with the conductivity of EO10-PFPE reaching 1.0×10^{-4} S cm^{-1} at 80 °C. Given the fact that the conductivity reported here is the apparent conductivity and the volume fraction of PEG phase is less than 100% (~ 85%, Table S1), we expect that the true

conductivity of PEG-rich phase in EO10-PFPE is much higher than the conductivity reported in Fig. 2d (see Figure S7 for normalized conductivity of EO10-PFPE).This enhanced conductivity could originate from the relatively low T_g (Fig. 1b) which facilitates the ion transport.[38] Another benefit of introducing PFPE into the polymer backbone is seen by the increased Na^+ transference number (t_{Na+}). As shown in Fig. 2e, t_{Na+} of EO10-PFPE is 0.48 at 80 ^oC, much higher than EO10-CTRL (0.33 at 80°C). Due to the higher t_{Na+} and higher conductivity, the EO10-PFPE shows increased Na^+ conductivity (total conductivity × t_{Na+}) of 4.7×10^{-5} S cm^{-1}, 1.5 times higher than that of EO10-CTRL electrolyte (Fig. 2f). The Vogel-Fulcher-Tamman (VFT) fitting results in Fig. 2e indicates that there is no significant change in activation energy in these two electrolytes. The role of PFPE segments is highlighted by the NMR results in Fig. 2h. As one moves from NaFSI to EO10-CTRL-NaFSI to EO10-PFPE-NaFSI, an upfield shift in ^{19}F NMR resonance is observed which correlates with stronger ion solvation or an increase in ion pairing, *i.e.* increased interactions between FSI anions and PFPE polymer in this case.[20, 21, 49–51] This anion-polymer interaction limits FSI mobility and enhances t_{Na+}, which is in good agreement with previous studies of lithium electrolytes as reported by Balsara and co-workers.[23, 47]

Electrochemical stability of the electrolyte materials is crucial to sustain high performance and reversibility of electrochemical reactions during Na battery operation. The CV results shown in Fig. 2i confirm a reversible plating and stripping process and absence of significant oxidation (< 4.0 V) when EO10-PFPE electrolyte is used. Furthermore, linear sweep voltammetry (LSV) shows the electrochemical stability window of EO10-PFPE is approximately 4.5 V (inset of Fig. 2i), sufficient for most Na battery applications.[52] It is noteable that compared with EO10-CTRL, the EO10-PFPE shows a much lower oxidation current until 5 V, indicative of superior oxidative stability under high voltage conditions. We attribute this increased oxidation stability to the formation of PFPE-rich domains with high oxidation stability.[21, 53] As suggested by Bao *et al*,[21] the formation of PFPE-rich domains via self-assembly limits the contact of ethylene oxide repeat units with the electrode surface and protects the electrolyte from further oxidation at high voltage. These results highlight the potential for introducing PFPE domains in PEG electrolytes and the benefits from formation of a phase-separated structure as an effective strategy for enhancing the electrochemical stability and Na^+ transport properties of polymer electrolytes.

Molecular dynamics (MD) simulations were then performed in order to further understand the interactions between NaFSI and the polymer matrix.[54] Therein, we separately studied the behavior of concentrated solutions of EO-PFPE and EO-CTRL in diethyl ether, with Na^+ and FSI^- ions. During the simulations, both polymers readily formed complexes with Na^+ and FSI^- ions with folded polymer structures being observed (Supplementary Figure S12-S13). Although the original experiments were conducted without the presence of an organic solvent, this approach allowed better equilibration of the polymer structure by increasing side-chains flexibility in the presence of solvent. Figures 3a-b show the different structures formed after 200 ns simulation time with the hydrophobic fluorinated chains closely packed at the surface, whereas the core of the assembly is composed of an ion-rich phase. For the EO-CTRL electrolyte, Na ions are evenly distributed in the whole polymer matrix, forming EO-Na^+ complexes while a distinct

phase separation is observed in the EO-PFPE electrolyte (Fig. 3c, Figure S14). It can also be observed that Na ions primarily locate in the PEG-rich phase, forming EO-Na^+ complexes, which explains the high dependence of T_g on NaFSI concentrations shown in the DSC results in Fig. 1b.

Based on the calculated trajectories, we determined the binding energies between different species in the system was calculated. Figure 3d compares the binding energies between NaFSI and different components within the electrolytes (also seen in Figure S15). Compared with EO-CTRL, there is evidence of weakened interactions between EO-PFPE polymer chains and Na^+ ions (-79.4 kcal mol^{-1} *vs* -98.3 kcal mol^{-1}) with the binding energy between EO-PFPE and FSI^- doubled. This suggests that the addition of PFPE moieties into a PEG matrix will help 'release' more Na^+ while restricting the mobility of FSI anions, leading to increased t_{Na+} (Fig. 2e).[55] Another benefit of using PFPE blocks is the decrease in association energy between Na^+ and FSI^-. This could be rationalized by the additional FSI-polymer interactions, which lowers the binding energy between Na and FSI ions.

Na Plating/Stripping Performance and Impedance Measurements of Symmetric Cells

The formation of a stable SEI layer between the electrolyte and the Na-metal anode is one of the most effective strategies for improving long-term cycling stability of Na-metal batteries, and to further inhibit short-circuits caused by Na dendrite growth.[52] To evaluate the electrochemical stability of the EO10-PFPE electrolyte against Na metal, symmetric Na/Na cells were assembled for testing Na plating/stripping performance, long-term stability and comparison with the EO10-CTRL electrolyte (Fig. 4). Impressively, the EO10-PFPE/PVDF composite exhibits extremely stable Na plating/striping behavior at high current density of 0.5 mA cm^{-2} (0.5 mAh cm^{-2}) for 200 cycles without significant voltage oscillation (green, Fig. 4b). In contrast, the EO10-CTRL electrolyte can only be cycled at a much lower current density of 0.1 mA cm^{-2} (0.1 mAh cm^{-2}). A severe voltage oscillation is observed, between 50–150 h in this case, suggesting the formation Na dendrites and an unstable SEI.[56] Further increase in the current density to 0.5 mA cm^{-2} leads to an immediately elevated overpotential and a final shorting failure of the symmetric cell in the control electrolyte (blue, Fig. 4b).

As discussed earlier, the EO10-CTRL electrolyte shows liquid-like behavior and the resultant PVDF composite is a soft and non-free-standing membrane (Figures S7 & S8), leading to cell failure, even at low current density. To eliminate this mechanical limitation and further confirm the stability of EO10-PFPE, composite electrolytes using a commercial Solupor separator were prepared and used to provide mechanical support. The Solupor separator has a similar porous structure to PVDF (Fig. 4c, SEM image). The performance of symmetric cells assembled with Sulopor-based EO10-PFPE and EO10-CTRL electrolytes was tested at 80 ^oC and is shown in Fig. 4d. In order to distinguish their different behavior, we designed a new protocol consisting of different current cycling and long-term cycling at high current density. These two symmetric cells both show the capability of cycling at different current density from

0.05 to 0.6 mA cm^{-2} (1 h plating/1 h stripping). After 140 h, the cells were cycled at constant current density of 0.5 mA cm^{-2}, but with a longer interval of 2 h (1.0 mAh cm^{-2}). Clearly, the EO10-CTRL/Solupor composite electrolyte exhibits a sudden short-circuit after only 100 cycles while the EO10-PFPE/Solupor composite electrolyte shows extremely stable cycling performance for 400 cycles (1000 h) under harsh cycling conditions of 1.0 mAh cm^{-2} per cycle. The superior stability with Na metal achieved by using the EO10-PFPE electrolyte is further confirmed by the evolution of the impedance spectra. The overall cell resistance (highlighted in dashed lines) of the Na/Na symmetric cell with EO10-CTRL/Solupor electrolyte continuously shifts to lower values followed by a dramatic decrease of overall resistance, indicative of cell failure due to short circuits (Fig. 4e). In sharp contrast, the symmetric cell assembled with EO10-PFPE/Solupor electrolyte demonstrates ultra-stable cell resistance during long-term cycling for over 1000 h (Fig. 4f). The extracted interfacial resistance summarized in Fig. 4g clearly demonstrates that a consistent value is maintained for the composite electrolyte with EO10-PFPE. The ultra-stable performance of the symmetric cells demonstrated by both composite electrolytes, EO10-PFPE/PVDF and EO10-PFPE/Solupor, therefore provides strong evidence of the formation of a stable SEI between the PFPE containing electrolyte and the Na metal anode.

As proposed in previous studies, any morphological changes at the anode surfaces caused by void formation, uneven metal deposition, dendrite growth or SEI formation will affect the overall resistance and final cell performance.[52, 57, 58] To further compare the changes in Na metal morphology during the plating/stripping process, Na/Cu cells with different electrolytes were tested. It should be noted that the majority of Na/Cu plating/stripping experiments performed previously are based on the use of liquid electrolytes, and the coulombic efficiency (CE) of dry solid electrolytes has been rarely reported.[5] Nevertheless, the EO10-PFPE composite electrolyte shows promising stability, up to 400 cycles (average CE = 89.7%) with much lower overpotential, while the EO10-CTRL electrolytes failed after 80 cycles (average CE = 82.8%, Figure S8a-c). To the best of our knowledge, this is the first plating/stripping demonstration of a solid-state Na/Cu cell for such a long time. Also, the lower overpotential convinces the efficient Na^+ transport of EO10-PFPE as confirmed in Fig. 2f. SEM images of the cycled Na electrode surfaces reveal that uneven Na deposits were formed on the Cu current collector (indicated by arrows in Fig. 5a) when the EO10-CTRL electrolyte was used. The enlarged view shown in Fig. 5b and energy dispersive spectroscopy (EDS) Na mapping in Fig. 5c further confirm the formation of dendritic Na, suggesting the failure of the Na/Cu cell was due to a short circuit. By contrast, a uniform deposition layer is maintained when EO10-PFPE was used (Fig. 5d). Thus, we can conclude that the incorporation of PFPE-moiety into PEG electrolyte greatly inhibits dendrite and void formation, resulting a stable SEI on Na metal surface (Fig. 5g-h). It should be also mentioned that the Na layer was densely deposited on the Cu current collector (Figs. 5e-f). This morphology is beneficial to minimize side reactions and limit SEI growth, which strongly supports the stable plating/stripping performance as demonstrated in Na/Na cycling tests in Fig. 4f. One may notice that the deposited Na layer in Fig. 5f is surprisingly thick, which likely arises from the accumulation of Na metal during long term cycling and the relatively low CE.

All-Solid-State Na-metal battery Performance

The electrochemical performance of the all-solid-state Na/NVP batteries with EO10-PFPE/PVDF composite electrolyte was evaluated and is shown in Fig. 6. The Na/NVP cell was cycled at C/10 for three cycles, then C/5, C/2, 1C, 2C and back to C/10 for five cycles to investigate the capability of the cell at different current densities (Fig. 6a). The cell shows an initial discharge capacity of 96.8 mAh g^{-1}, and a relatively low initial CE of around 90% at C/10, which could be related to SEI formation.[59] When the current density was increased to C/5, C/2, 1C and 2C, the discharge capacities were 95.9, 93.1, 91.2 and 87.7 mAh g^{-1}, respectively. The cell promptly recovered to a capacity of 96.3 mAh g^{-1} when the C rate was returned to C/10, which indicates a superior capability of cycling at various C rates. More impressively, the all-solid-state Na-metal cell shows extremely long-term stability and high CE at 2C (≈ 0.2 mA cm^{-2}). In particular, the discharge capacity only drops from 87.2 to 85.0 mAh g^{-1} after more than 940 cycles with a capacity retention of 97.5% (average capacity loss rate of 0.0026%) with an average CE higher than 99.9%. The superior cycling stability at high C rate is also confirmed by the charge/discharge profiles in Fig. 6b and it is apparent that the charge/discharge curves during the first 500 cycles essentially overlap. In terms of battery resistance, the recorded EIS spectra during 2C cycling measurements are shown in Fig. 6c. It is observed that the overall cell resistance increases after 100 cycles, which could result from increased interfacial resistance (e.g. cathode-electrolyte-interphase formation[60]) at high current density. Another important observation from Fig. 6c is that the cell resistance only increases from around 700 to 790 Ohm during the subsequent cycles, which again highlights the capability of the EO10-PFPE/PVDF electrolyte to sustain high-rate cycling with high stability. Further evidence of long-term stability of the electrolyte is also provided by additional cells cycled at a lower rate of C/2 shown in Figure S9.

The outstanding performance of EO10-PFPE composite electrolyte demonstrated in the study is highlighted by comparison with previous studies based on other polymer or composite electrolytes (Fig. 7, Table S3).[18, 61–72] It is clear that the EO10-PFPE composite electrolyte shows the highest capacity retention (97.5% after 940 cycles) and outstanding capacity output in Na-metal full cells and Na/Na cells.

Conclusions

We have demonstrated an ultra-stable all-solid-state Na-metal battery achieved using a perfluoropolyether (PFPE)-based block copolymer as the solid electrolyte. Our results confirm that the incorporation of PFPE domains segments assist the formation of a self-assembled solid phase, leading to improved mechanical properties with enhanced storage modulus. Additionally, this phase separated microstructure shows synergistic benefits for improving electrolyte performance with molecular dynamics (MD) simulations confirming that the PFPE polymer has weakened interactions with Na ions while enhanced interactions with FSI anions. As a consequence, both the Na^+ transference number and Na^+ conductivity are increased which leads to the composite block copolymer electrolyte showing remarkable long-term cycling stability with a high capacity of 1.0 mAh cm^{-2} and excellent reversibility in long-term Na plating/stripping tests. Finally, the assembled solid-state Na-metal batteries (with $Na_3V_2(PO_4)_3$ cathodes) demonstrate stable rate capability and outstanding charge/discharge reversibility (CE = 99.91%) at 2C (≈ 0.2 mA cm^{-2}) after more than 900 cycles at elevated temperature of 80 ^oC.

Experimental

Materials

The hydroxy-terminated perfluorinated poly(propylene ether) (PFPE-OH, *M*w ~ 1300 g/mol, CAS Number: 1980064-28-5) was purchased from Apollo Scientific Ltd., UK. Oligo(ethylene glycol) methyl ether acrylate (OEGA, *M*w = 480 g/mol) purchased from Sigma Aldrich was passed through basic alumina columns to remove inhibitors before use. The initiator 2,2'-azobis(2-methylpropionitrile) (AIBN) was recrystallized twice from methanol prior to use. The RAFT agent 2-(butylthiocarbonothioylthio)propionic acid (BTPA) was prepared according to a previously reported procedure.[73] V_2O_5 (99.9%) and $H_2C_2O_4$ (anhydrous) were and all other chemicals were purchased from Sigma Aldrich and used as received.

Synthesis of CTRL- and PFPE-polymers

Synthesis of CTRL- and PFPE-polymers was performed according to reported methods.[25] In a typical experiment for preparing EO10-PFPE, PFPE macro-RAFT agent (187 mg, 0.11 mmol), PEGA (770 mg, 1.6 mmol), and AIBN (3.28 mg, 0.020 mmol) were dissolved in trifluorotoluene (2 mL) and sealed in a 10 mL flask fitted with a magnetic stirrer bar. The solution was then deoxygenated by purging thoroughly with nitrogen for 15 min, heated to 65 °C in an oil bath, and allowed to react for ≈ 4 h with conversion at ≈ 70%. Upon completing the reaction, the solution was precipitated into hexane three times. The precipitate was then dried in a vacuum oven at 60 °C for 12 h, yielding a yellow viscous solid. Polymers with a range of PFPE compositions were prepared under identical conditions apart from differences in the initial feed amount between PEGA and PFPE macro-RAFT agent. The CTRL sample was prepared with the same procedure in the absence of PFPE macro-RAFT agent.

Polymer electrolyte preparation

The polymer electrolytes were prepared by solvent casting method as described in previous literature.[74, 75] Particularly, PFPE polymer was dried at 50 ^{o}C under vacuum for two days and dissolved in dry acetonitrile together with dry NaFSI salt. The salt concentration was determined by the molar ratio of PEGA groups and NaFSI salt. In this study, high concentration of NaFSI salt was used, and the EO/Na ratio was kept as 10/1 and 5/2, corresponding to one and two Na^+ per PEGA side chain, respectively. For battery tests, composite electrolytes with incorporation of PVDF fibers were used, the composite electrolytes were prepared by casting prepared polymer solution with PVDF matrix (≈ 100 µm of thickness) according to our previous work.[74] The composites with Solupor

separators were prepared the same way. The composites were finally dried under vacuum at least for 2 days in order to completely remove solvent and water residuals.

Synthesis of carbon-coated $Na_3V_2(PO_4)_3$ (NVP)

The synthesis of carbon-coated $Na_3V_2(PO_4)_3$ (NVP) was performed as described elsewhere.[76] In a typical synthesis, V_2O_5 and $H_2C_2O_4$ were dissolved into deionized water and vigorously stirred at 70 °C for 1 h in order to obtain a VOC_2O_4 solution. Sequentially, NaH_2PO_4 and glucose were added to VOC_2O_4 solution and the mixture was kept under stirring for additional 10 minutes. Afterwards, N-propanol was further added into VOC_2O_4 solution and was left stirring for 30 min. The NVP precursor was obtained by removing the solvent by the aid of a rotary evaporator and the as-obtained solid was further dried under vacuum at 60 °C for 12h. Finally, $Na_3V_2(PO_4)_3$/C micro-composites were obtained by pre-treating the precursor at 400 °C for 4 h followed by annealing at 750 °C for 8 h under inert atmosphere (Ar) at a heating rate of 5 °C/min.

Cathode preparation.

Cathode electrodes were prepared by using a slurry composed of 60 wt% of active material $Na_3V_2(PO_4)_3$/C), 30wt% of polymer electrolyte binder and 10 wt% of conductive carbon (C65, Timcal). The slurry was obtained by initially dissolving the binder in NMP (*N*-2-methyl-pyrrolidinone) in a small beaker followed by mild stirring for 30 min. In parallel, a pre-weighted amount of NVP cathode material and carbon C65 were ground in an agate mortar for 30 minutes. Afterwards, the ground solid mixture was added to the beaker containing the pre-dissolved binder and a few extra drops of NMP solvent were added to the beaker. In order to obtain a homogeneous slurry, the beaker was left stirring overnight. Subsequently, the viscous slurry was cast onto aluminum foil by using of a doctor blade. The as-obtained film was initially dried at 60°C under vacuum for 24h and then punched into disks to obtain the electrodes. Before being transferred to the glovebox, the electrodes were further dried in schlenk line for 12 h at 80 °C using an air tight vessel. After transferring the vessel to the glovebox (Kiyon, Korea), a set of electrodes (with diameter of 8mm) were weighed and the average active mass loading of the electrodes were around 1.0 mg cm^{-2}.

Characterization

Differential scanning calorimetry (DSC). A Netzsch DSC (214 Polyma) was used to investigate the thermal behaviors of the electrolytes with and without salt. For DSC measurements, an Al pan was used and 5−10 mg of material was sealed in an argon glovebox. Prior to measurements, the DSC instrument was calibrated by using cyclohexane. All samples were cooled to −120 °C first and then heated to 180 °C with a cooling and

heating rate of 10 °C/min. The DSC scans reported in this study were extracted from the second heating scan.

NMR spectroscopy. Solution-state ^{1}H and ^{19}F NMR spectra were recorded on a Bruker Avance 400 MHz (9.4 T) spectrometer in $CDCl_3$. Chemical shifts (δ) in ^{1}H NMR spectra are reported in ppm relative to the residual $CHCl_3$ (7.26 ppm). Solid-state NMR spectra were acquired on a Bruker 300 MHz spectrometer.

Small-angle X-ray scattering (SAXS). SAXS measurements of bulk samples were conducted using a custom-built SAXS diffractometer at the Materials Research Laboratory (MRL) X-ray facility (University of California, Santa Barbara). For these experiments, 1.54 Å Cu Kα X-rays were generated using a Genix 50 W X-ray microsource (50 µm micro-focus) equipped with FOX2D collimating multilayer optics (Xenocs, France) and high efficiency scatterless single crystal/metal hybrid slits. Samples were prepared using capillaries for SAXS experiments.

Dynamic mechanical thermal analysis (DMTA). Rheological experiments were performed on either TA Instruments ARES dynamic mechanical spectrometer using the 25 mm parallel plate geometry with a gap of approximately 1 mm for most experiments. Strain sweep experiments determined the linear viscoelastic region. Isothermal frequency sweeps (100–0.1 rad/sec) were performed in the linear viscoelastic regime, as confirmed by strain sweep measurements at selected temperatures. Temperature was controlled using the forced convection oven attachment.

Electrochemical measurements and full cell tests. Ionic conductivity. The ionic conductivities of PFPE and control electrolytes were measured using electrochemical impedance spectroscopy (EIS) on a Solartron instrument. The frequency range was set from 1 MHz - 0.1 mHZ with an amplitude voltage of 10 mV. The samples were sealed in a home-made barrel cell in an Ar-glove box. The temperature was controlled via a Eurotherm 2204 controller, and the temperature range was from 30 to 100 °C (10 ºC interval). Before each EIS test, the temperature was stabilized for 40 minutes.

Coulombic efficiency. The Na/Cu cells were assembled in Ar-filled glovebox. The diameters of Cu and Na disks are 10mm and 8 mm, respectively. For each cycle, the experiments were done by plating 0.2 mAh cm^{-2} of Na on Cu electrode (1 hour with current density of 0.2 mA cm-2) then followed by a stripping process at a current density of 0.1 mA cm^{-2} to a cut-off voltage of 1.0 V. All experiments were done at 80 ºC.

Na^+ transference number (t_{Na+}). The transference number was determined by the method reported previously, and was calculated by the following formula:

$$t_{Na+} = \frac{R_{cell}}{R_{DC}} = \frac{R_{cell}}{\frac{V_{DC}}{I_{DC}}}$$

Where the R_{cell} is the total resistance determined by EIS before DC polarization. The V_{DC} is the applied polarization voltage of 10 mV and the steady state current I_{DC} is obtained after 4 hours of stabilization.

To determine the R_{cell}, the following equivalent circuit is used:

Where R_1 is the bulk resistance of electrolyte material. R_2 and R_3 represent the resistance related with two electrode surfaces.

$Na/Na_3V_2(PO_4)_3$ battery tests. All-solid-state sodium-metal batteries comprising the NVP cathode were assembled in CR 2032 coin cells inside the Ar-filled glovebox (O_2 <0.1 ppm, H_2O <0.1 ppm). The sodium metal foil (Merck) was rolled and brushed, then cut into anode disks with diameter of 8 mm (area of ~0.5 cm^2) as anode. Full cells were cycled in a VMP-3 potentiostat in a potential range of 2.5-3.8 V at 80 °C.

Theoretical calculations.

Molecular dynamic (MD) simulations. The molecular structures studied were prepared in GaussView and their atom types and charges were obtained from the CHARMM force field. The CHARMM general force field[77, 78] was implemented for the bond, angle, and dihedral parameters of the ligands and solvent molecules. Non-bonding interactions between these molecules, such as vdW attraction and steric repulsion were described by the Lennard-Jones (LJ) potential,

$$U_{LJ}(r) = \varepsilon\left[\left(\frac{r_{min}}{r}\right)^{12} - 2\left(\frac{r_{min}}{r}\right)^{6}\right],$$

where ε is the minimum (negative) energy of this coupling, and r is a distance where has a local minimum, which are provided by the CHARMM force field. Here, the r^{-12} term describes an atomic repulsion, due to overlapping electron orbitals, and the r^{-6} term represents the vdW attractive coupling. The LJ potential implemented in NAMD has a cutoff distance of 1 nm. The electrostatic coupling between ions and partially charged atoms, also

contribute to the non-bonding interactions, has the same cutoff distance as the LJ potential, but its long-range part is calculated by the PME method[79] in the presence of periodic boundary conditions. The molecular dynamic (MD) simulations of the prepared systems were performed with NAMD[80] in an NPT ensemble at T = 298 K and P = 1 atm, using the Langevin dynamics with a damping constant of $\gamma_{\mathrm{Lang}} = 0.1\ \mathrm{ps}^{-1}$ and a time step of 2 fs.

For MD simulations in the organic solvent droplet, in order to overcome a potentially poor polymer mobility in the simulations, we analyzed the behavior of the same polymer in diethyl ether as a solvent, leading to the well-equilibrated polymer-ion assembly. We run two analogous MD simulations with (i) EO5-PFPE and (ii) EO5-CTRL, both in diethyl ether droplets (initially in a form of 7 × 7 × 7 nm cubes, which were placed in 30 × 30 × 30 nm vacuum boxes), composed of:

i. 13 EO5-PFPE molecules, 1987 diethyl ether molecules, 65 Na+ cations and the same number of FSI– anions. These numbers yield concentration of the polymer equal to 27.0% by mass (63.0 mM); EO-to-Na^+ ratio was equal to 8:1.
ii. 13 EO5-CTRL molecules, 1987 diethyl ether molecules, 65 Na^+ cations and the same number of FSI^- anions. These numbers yield the same molar concentration of the polymer as in (i), 63.0 mM, and 17.8% by mass; EO-to-Na+ ratio was also equal to 8:1.

Binding energy calculations. Based on the obtained trajectories, we calculated the binding energies between the polymer chains, Na^+-polymer, FSI-polymer and Na^+-FSI pairs using the NAMD Energy toolkit. The calculations were run for the last 1 ns of the 200 ns simulations.

Declarations

Acknowledgements

The authors acknowledge the support of the Australia-India Strategic Research Fund (AISRF 48515). M. F thanks the Australian Research Council for their Australian Laureate Fellowship program. The research reported here was partially supported by the National Science Foundation (NSF) through the Materials Research Science and Engineering Center at UC Santa Barbara, DMR-1720256 (IRG-2). A.K.W. and C.Z. acknowledge support from the Australian Research Council (CE140100036) and National Health and Medical Research Council for an Early Career Fellowship (APP1157440 to C.Z.). The Australian National Fabrication Facility, Queensland Node, is also acknowledged for access to some items of equipment.

References

1. Q. Zhao, W. Zhao, C. Zhang, Y. Wu, Q. Yuan, A. K. Whittaker and X. S. Zhao, *Energy & Fuels*, 2020, **34**, 5099-5105.
2. V. Palomares, P. Serras, I. Villaluenga, K. B. Hueso, J. Carretero-González and T. Rojo, *Energy & Environmental Science*, 2012, **5**, 5884-5901.
3. X.-B. Cheng, R. Zhang, C.-Z. Zhao and Q. Zhang, *Chemical Reviews*, 2017, **117**, 10403-10473.
4. C. Zhao, Y. Lu, J. Yue, D. Pan, Y. Qi, Y.-S. Hu and L. Chen, *Journal of Energy Chemistry*, 2018, **27**, 1584-1596.
5. Y. Zhao, K. R. Adair and X. Sun, *Energy & Environmental Science*, 2018, **11**, 2673-2695.
6. Q. Zhao, D. Yang, C. Zhang, X.-H. Liu, X. Fan, A. K. Whittaker and X. S. Zhao, *ACS Applied Materials & Interfaces*, 2018, **10**, 43730-43739.
7. B. L. Ellis and L. F. Nazar, *Current Opinion in Solid State and Materials Science*, 2012, **16**, 168-177.
8. Y. Lu, L. Li, Q. Zhang, Z. Niu and J. Chen, *Joule*, 2018, **2**, 1747-1770.
9. T. Famprikis, P. Canepa, J. A. Dawson, M. S. Islam and C. Masquelier, *Nature Materials*, 2019, **18**, 1278-1291.
10. L. Porz, T. Swamy, B. W. Sheldon, D. Rettenwander, T. Frömling, H. L. Thaman, S. Berendts, R. Uecker, W. C. Carter and Y.-M. Chiang, *Advanced Energy Materials*, 2017, **7**, 1701003.
11. J. Li, H. Zhu, X. Wang, M. Armand, D. R. MacFarlane and M. Forsyth, *Electrochimica Acta*, 2015, **175**, 232-239.
12. J. Yang, H. Zhang, Q. Zhou, H. Qu, T. Dong, M. Zhang, B. Tang, J. Zhang and G. Cui, *ACS Applied Materials & Interfaces*, 2019, **11**, 17109-17127.
13. J. Li, H. Zhu, X. Wang, D. R. MacFarlane, M. Armand and M. Forsyth, *Journal of Materials Chemistry A*, 2015, **3**, 19989-19995.
14. I. Aldalur, X. Wang, A. Santiago, N. Goujon, M. Echeverría, M. Martínez-Ibáñez, M. Piszcz, P. C. Howlett, M. Forsyth, M. Armand and H. Zhang, *Journal of Power Sources*, 2020, **448**, 227424.
15. M. Forsyth, L. Porcarelli, X. Wang, N. Goujon and D. Mecerreyes, *Accounts of Chemical Research*, 2019, **52**, 686-694.
16. X. Wang, R. Kerr, F. Chen, N. Goujon, J. M. Pringle, D. Mecerreyes, M. Forsyth and P. C. Howlett, *Advanced Materials*, 2020, **32**, 1905219.
17. J. Mindemark, M. J. Lacey, T. Bowden and D. Brandell, *Progress in Polymer Science*, 2018, **81**, 114-143.
18. L. Liu, X. Qi, S. Yin, Q. Zhang, X. Liu, L. Suo, H. Li, L. Chen and Y.-S. Hu, *ACS Energy Letters*, 2019, **4**, 1650-1657.
19. X. Fan, X. Ji, L. Chen, J. Chen, T. Deng, F. Han, J. Yue, N. Piao, R. Wang, X. Zhou, X. Xiao, L. Chen and C. Wang, *Nature Energy*, 2019, **4**, 882-890.
20. Z. Yu, H. Wang, X. Kong, W. Huang, Y. Tsao, D. G. Mackanic, K. Wang, X. Wang, W. Huang, S. Choudhury, Y. Zheng, C. V. Amanchukwu, S. T. Hung, Y. Ma, E. G. Lomeli, J. Qin, Y. Cui and Z. Bao, *Nature Energy*, 2020, **5**, 526-533.

21. C. V. Amanchukwu, Z. Yu, X. Kong, J. Qin, Y. Cui and Z. Bao, *Journal of the American Chemical Society*, 2020, **142**, 7393-7403.
22. L. Suo, W. Xue, M. Gobet, S. G. Greenbaum, C. Wang, Y. Chen, W. Yang, Y. Li and J. Li, *Proceedings of the National Academy of Sciences*, 2018, **115**, 1156.
23. D. B. Shah, K. R. Olson, A. Karny, S. J. Mecham, J. M. DeSimone and N. P. Balsara, *Journal of The Electrochemical Society*, 2017, **164**, A3511-A3517.
24. L. Qiao, X. Judez, T. Rojo, M. Armand and H. Zhang, *Journal of The Electrochemical Society*, 2020, **167**, 070534.
25. C. Zhang, S. S. Moonshi, Y. Han, S. Puttick, H. Peng, B. J. A. Magoling, J. C. Reid, S. Bernardi, D. J. Searles, P. Král and A. K. Whittaker, *Macromolecules*, 2017, **50**, 5953-5963.
26. C. Zhang, S. S. Moonshi, W. Wang, H. T. Ta, Y. Han, F. Y. Han, H. Peng, P. Král, B. E. Rolfe, J. J. Gooding, K. Gaus and A. K. Whittaker, *ACS Nano*, 2018, **12**, 9162-9176.
27. S. S. Moonshi, C. Zhang, H. Peng, S. Puttick, S. Rose, N. M. Fisk, K. Bhakoo, B. W. Stringer, G. G. Qiao, P. A. Gurr and A. K. Whittaker, *Nanoscale*, 2018, **10**, 8226-8239.
28. C. Zhang, T. Liu, W. Wang, C. A. Bell, Y. Han, C. Fu, H. Peng, X. Tan, P. Král, K. Gaus, J. J. Gooding and A. K. Whittaker, *ACS Nano*, 2020, **14**, 7425-7434.
29. C. Zhang, L. Li, F. Y. Han, X. Yu, X. Tan, C. Fu, Z. P. Xu and A. K. Whittaker, *Small*, 2019, **15**, 1902309.
30. C. Zhang, R. J. P. Sanchez, C. Fu, R. Clayden-Zabik, H. Peng, K. Kempe and A. K. Whittaker, *Biomacromolecules*, 2019, **20**, 365-374.
31. C. Fu, B. Demir, S. Alcantara, V. Kumar, F. Han, H. G. Kelly, X. Tan, Y. Yu, W. Xu and J. Zhao, *Angewandte Chemie*, 2020, **132**, 4759-4765.
32. C. Fu, Y. Yu, X. Xu, Q. Wang, Y. Chang, C. Zhang, J. Zhao, H. Peng and A. K. Whittaker, *Progress in Polymer Science*, 2020, **108**, 101286.
33. E. Önal, C. Zhang, D. Davarcı, Ü. İşci, G. Pilet, A. K. Whittaker and F. Dumoulin, *Tetrahedron Letters*, 2018, **59**, 521-523.
34. X. Tan, J. Zhong, C. Fu, H. Dang, Y. Han, P. Král, J. Guo, Z. Yuan, H. Peng, C. Zhang and A. K. Whittaker, *Macromolecules*, 2021, DOI: 10.1021/acs.macromol.1c00096.
35. T. Li, X.-Q. Zhang, P. Shi and Q. Zhang, *Joule*, 2019, **3**, 2647-2661.
36. N. A. Stolwijk, C. Heddier, M. Reschke, M. Wiencierz, J. Bokeloh and G. Wilde, *Macromolecules*, 2013, **46**, 8580-8588.
37. R. He and T. Kyu, *Macromolecules*, 2016, **49**, 5637-5648.
38. T. Kinsey, K. Glynn, T. Cosby, C. Iacob and J. Sangoro, *ACS Applied Materials & Interfaces*, 2020, **12**, 44325-44334.
39. W. K. Kipnusu, M. M. Elmahdy, M. Elsayed, R. Krause-Rehberg and F. Kremer, *Macromolecules*, 2019, **52**, 1864-1873.
40. K. Adrjanowicz and M. Paluch, *Physical Review Letters*, 2019, **122**, 176101.
41. S. Napolitano and M. Wübbenhorst, *Nature Communications*, 2011, **2**, 260.

42. T. Zhang, K. I. Winey and R. A. Riggleman, *Macromolecules*, 2019, **52**, 217-226.
43. C. Zhang, M. W. Bates, Z. Geng, A. E. Levi, D. Vigil, S. M. Barbon, T. Loman, K. T. Delaney, G. H. Fredrickson, C. M. Bates, A. K. Whittaker and C. J. Hawker, *Journal of the American Chemical Society*, 2020, **142**, 9843-9849.
44. W. K. Kipnusu, M. Elsayed, W. Kossack, S. Pawlus, K. Adrjanowicz, M. Tress, E. U. Mapesa, R. Krause-Rehberg, K. Kaminski and F. Kremer, *The Journal of Physical Chemistry Letters*, 2015, **6**, 3708-3712.
45. Z. Yu, D. G. Mackanic, W. Michaels, M. Lee, A. Pei, D. Feng, Q. Zhang, Y. Tsao, C. V. Amanchukwu, X. Yan, H. Wang, S. Chen, K. Liu, J. Kang, J. Qin, Y. Cui and Z. Bao, *Joule*, 2019, **3**, 2761-2776.
46. J. Lopez, D. G. Mackanic, Y. Cui and Z. Bao, *Nature Reviews Materials*, 2019, **4**, 312-330.
47. D. H. C. Wong, J. L. Thelen, Y. Fu, D. Devaux, A. A. Pandya, V. S. Battaglia, N. P. Balsara and J. M. DeSimone, *Proceedings of the National Academy of Sciences*, 2014, **111**, 3327.
48. D. H. C. Wong, A. Vitale, D. Devaux, A. Taylor, A. A. Pandya, D. T. Hallinan, J. L. Thelen, S. J. Mecham, S. F. Lux, A. M. Lapides, P. R. Resnick, T. J. Meyer, R. M. Kostecki, N. P. Balsara and J. M. DeSimone, *Chemistry of Materials*, 2015, **27**, 597-603.
49. A. V. Cresce, S. M. Russell, O. Borodin, J. A. Allen, M. A. Schroeder, M. Dai, J. Peng, M. P. Gobet, S. G. Greenbaum, R. E. Rogers and K. Xu, *Physical Chemistry Chemical Physics*, 2017, **19**, 574-586.
50. C. Zhang, D. S. Kim, J. Lawrence, C. J. Hawker and A. K. Whittaker, *ACS Macro Letters*, 2018, **7**, 921-926.
51. C. Zhang, H. Peng and A. K. Whittaker, *Journal of Polymer Science Part A: Polymer Chemistry*, 2014, **52**, 2375-2385.
52. Y. Tian, Y. Sun, D. C. Hannah, Y. Xiao, H. Liu, K. W. Chapman, S.-H. Bo and G. Ceder, *Joule*, 2019, **3**, 1037-1050.
53. Z. Zhang, L. Hu, H. Wu, W. Weng, M. Koh, P. C. Redfern, L. A. Curtiss and K. Amine, *Energy & Environmental Science*, 2013, **6**, 1806-1810.
54. C. Zhang, S. S. Moonshi, H. Peng, S. Puttick, J. Reid, S. Bernardi, D. J. Searles and A. K. Whittaker, *ACS Sensors*, 2016, **1**, 757-765.
55. L. Cong, J. Liu, M. Armand, A. Mauger, C. M. Julien, H. Xie and L. Sun, *Journal of Power Sources*, 2018, **380**, 115-125.
56. T. Pathirana, R. Kerr, M. Forsyth and P. C. Howlett, *Journal of The Electrochemical Society*, 2020, **167**, 120526.
57. B. Liu, J.-G. Zhang and W. Xu, *Joule*, 2018, **2**, 833-845.
58. Y. Xiang, G. Zheng, Z. Liang, Y. Jin, X. Liu, S. Chen, K. Zhou, J. Zhu, M. Lin, H. He, J. Wan, S. Yu, G. Zhong, R. Fu, Y. Li and Y. Yang, *Nature Nanotechnology*, 2020, **15**, 883-890.
59. Y. Xiao, J.-Y. Hwang, I. Belharouak and Y.-K. Sun, *ACS Energy Letters*, 2017, **2**, 364-372.
60. J.-N. Zhang, Q. Li, Y. Wang, J. Zheng, X. Yu and H. Li, *Energy Storage Materials*, 2018, **14**, 1-7.
61. Q. Ma, J. Liu, X. Qi, X. Rong, Y. Shao, W. Feng, J. Nie, Y.-S. Hu, H. Li, X. Huang, L. Chen and Z. Zhou, *Journal of Materials Chemistry A*, 2017, **5**, 7738-7743.

62. C. Ma, K. Dai, H. Hou, X. Ji, L. Chen, D. G. Ivey and W. Wei, *Advanced Science*, 2018, **5**, 1700996.
63. Y. Yao, Z. Wei, H. Wang, H. Huang, Y. Jiang, X. Wu, X. Yao, Z.-S. Wu and Y. Yu, *Advanced Energy Materials*, 2020, **10**, 1903698.
64. W. Zhou, H. Gao and J. B. Goodenough, *Advanced Energy Materials*, 2016, **6**, 1501802.
65. S. Bag, C. Zhou, S. Reid, S. Butler and V. Thangadurai, *Journal of Power Sources*, 2020, **454**, 227954.
66. W. Zhou, Y. Li, S. Xin and J. B. Goodenough, *ACS Central Science*, 2017, **3**, 52-57.
67. Y.-B. Niu, Y.-X. Yin, W.-P. Wang, P.-F. Wang, W. Ling, Y. Xiao and Y.-G. Guo, *CCS Chemistry*, **2**, 589-597.
68. X. Yu, L. Xue, J. B. Goodenough and A. Manthiram, *ACS Materials Letters*, 2019, **1**, 132-138.
69. Y. Zheng, Q. Pan, M. Clites, B. W. Byles, E. Pomerantseva and C. Y. Li, *Advanced Energy Materials*, 2018, **8**, 1801885.
70. S. Malunavar, X. Wang, F. Makhlooghiazad, M. Armand, M. G. Mestres, P. Howlett and M. Forsyth, *Journal of Physics: Materials*, 2021, **submitted**.
71. Q. Zhang, Y. Lu, H. Yu, G. Yang, Q. Liu, Z. Wang, L. Chen and Y.-S. Hu, *Journal of The Electrochemical Society*, 2020, **167**, 070523.
72. J.-F. Wu, Z.-Y. Yu, Q. Wang and X. Guo, *Energy Storage Materials*, 2020, **24**, 467-471.
73. C. J. Ferguson, R. J. Hughes, D. Nguyen, B. T. T. Pham, R. G. Gilbert, A. K. Serelis, C. H. Such and B. S. Hawkett, *Macromolecules*, 2005, **38**, 2191-2204.
74. X. Wang, F. Chen, G. M. A. Girard, H. Zhu, D. R. MacFarlane, D. Mecerreyes, M. Armand, P. C. Howlett and M. Forsyth, *Joule*, 2019, **3**, 2687-2702.
75. X. Wang, G. M. A. Girard, H. Zhu, R. Yunis, D. R. MacFarlane, D. Mecerreyes, A. J. Bhattacharyya, P. C. Howlett and M. Forsyth, *ACS Applied Energy Materials*, 2019, **2**, 6237-6245.
76. Y. Li, Q. An, Y. Cheng, Y. Liang, Y. Ren, C.-J. Sun, H. Dong, Z. Tang, G. Li and Y. Yao, *Nano Energy*, 2017, **34**, 188-194.
77. K. Vanommeslaeghe, E. Hatcher, C. Acharya, S. Kundu, S. Zhong, J. Shim, E. Darian, O. Guvench, P. Lopes, I. Vorobyov and A. D. Mackerell Jr, *Journal of Computational Chemistry*, 2010, **31**, 671-690.
78. W. Yu, X. He, K. Vanommeslaeghe and A. D. MacKerell Jr, *Journal of Computational Chemistry*, 2012, **33**, 2451-2468.
79. P. mesh Ewald, *J. Chem. Phys*, 1993, **98**, 10089-10092.
80. J. C. Phillips, R. Braun, W. Wang, J. Gumbart, E. Tajkhorshid, E. Villa, C. Chipot, R. D. Skeel, L. Kalé and K. Schulten, *Journal of Computational Chemistry*, 2005, **26**, 1781-1802.

Figures

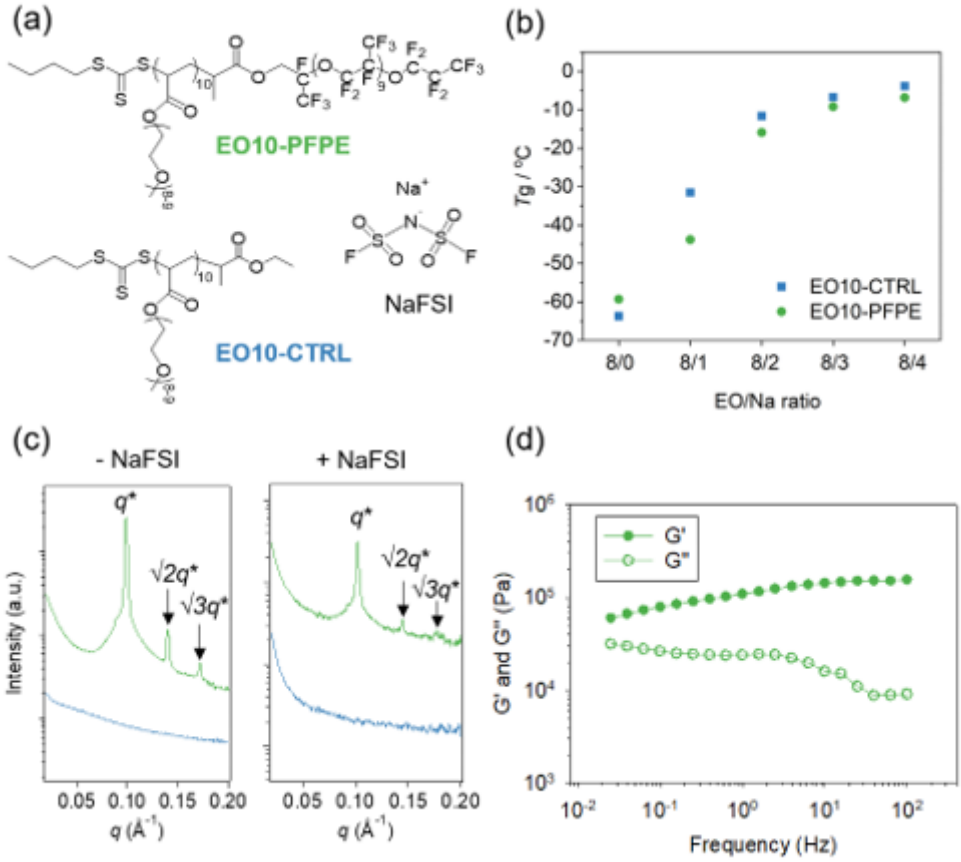

Figure 1

Chemical structures as well as physical and self-assembly properties of PFPE-based polymer electrolytes. (a) Chemical structures of poly(PEGA)10-PFPE (EO10-PFPE, green), control homopolymer poly(PEGA)10 (EO10-CTRL, blue) and NaFSI salt (red). (b) Dependence of glass transition temperature (Tg) of PEG on EO/Na ratios. (c) SAXS profiles showing self-assembled structures of EO10-CTRL and EO10-PFPE with or without NaFSI at 80 °C. (EO/Na = 8/2, molar ratio). (d) Changes in storage modulus (G') and loss modulus (G") of EO10-PFPE as a function of frequency at 80 °C.

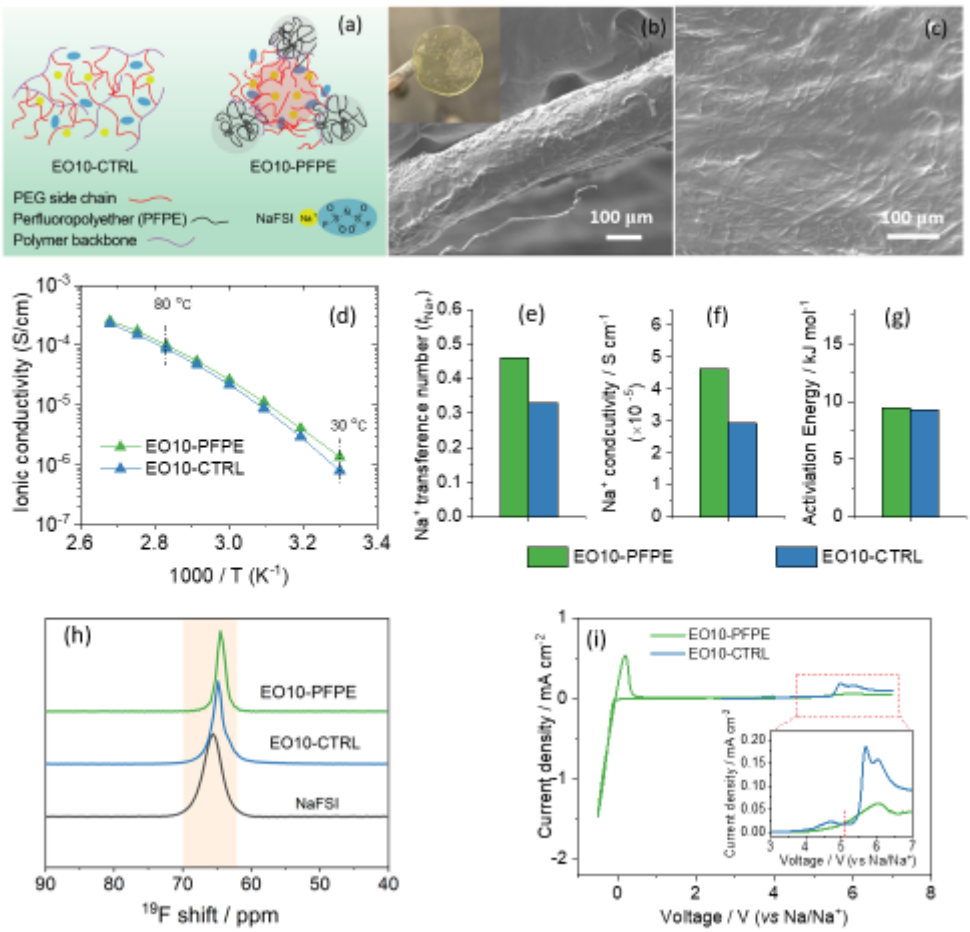

Figure 2

(a) Schematic illustration of proposed microstructures for EO10-CTRL and EO10-PFPE electrolytes as suggested by SAXS data in Figure 1c. (b) Cross-sectional SEM image of EO10-PFPE composite SPE. Inset is the photo of a free-standing membrane. (c) Surface SEM image of EO10-PFPE composite SPE. (d) Comparison of ionic conductivity of EO10-PFPE and EO10-CTRL composite electrolytes. (e-f) Comparison of Na+ transference number (tNa+), Na+ conductivity and activation energy (Ea) of EO10-PFPE and EO10-CTRL electrolytes. tNa+ was reported at 80 oC. (h) 19F NMR spectra of EO10-PFPE, EO10-CTRL electrolytes and NaFSI salt. (i) Cyclic voltammetry (CV) and linear sweep voltammetry (LSV) profiles of EO10-PFPE composite SPE. The LSV scan of EO10-CTRL composite electrolyte is also compared. The scanning rate is 1 mV/s at 80 oC.

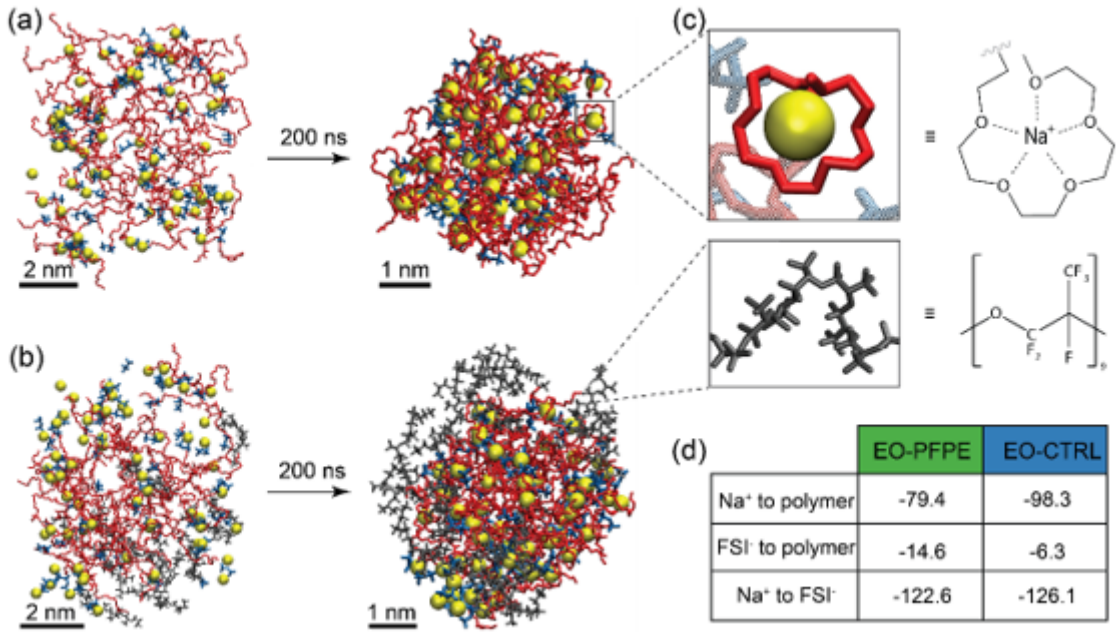

	EO-PFPE	EO-CTRL
Na^+ to polymer	-79.4	-98.3
FSI^- to polymer	-14.6	-6.3
Na^+ to FSI^-	-122.6	-126.1

Figure 3

MD simulations of (a) EO-CTRL polymer electrolyte and (b) EO-PFPE polymer electrolyte. The EO/Na+ ratio is equal to 8/1. Na+ = yellow spheres; FSI– = blue; EO chains = red; fluorinated fragment of the polymer = grey. (c) Example of crown ether-like complex between Na+ cations and EO units of the polymer. (d) The calculated binding energies between polymer-polymer, Na+-polymer, FSI–polymer and Na+-FSI- for last 1 ns of 200 ns simulation, normalized per 1 mole of ion.

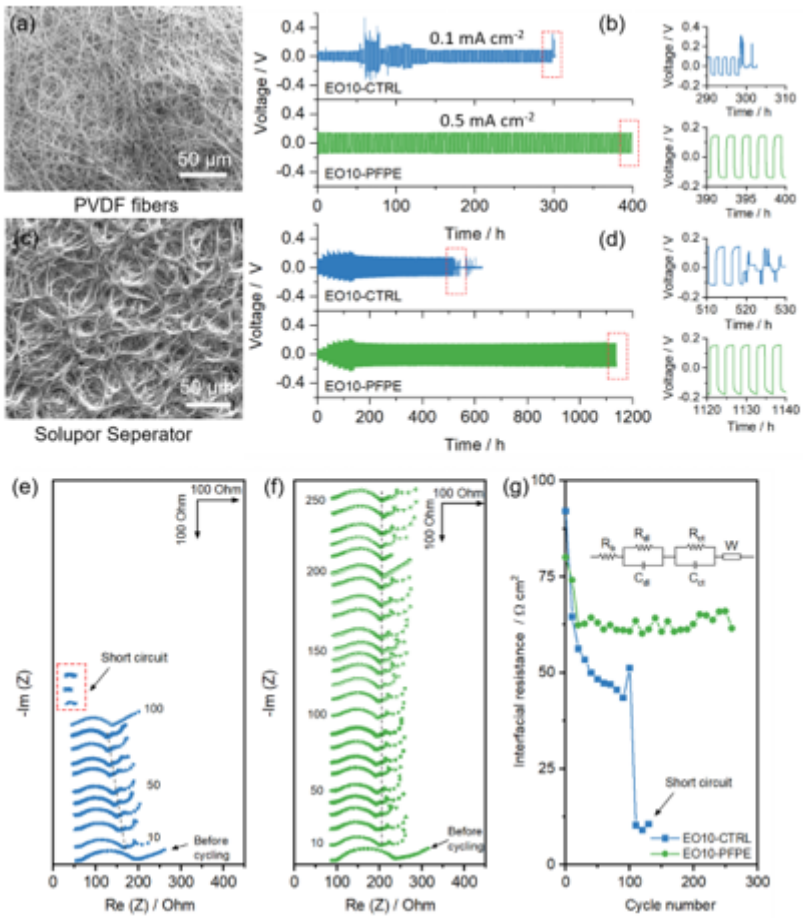

Figure 4

(a) SEM image of PVDF electrospun nanofibers and (b) plating/stripping performance of Na/Na symmetrical cells using composite electrolytes based on PVDF nanofiber separator. The applied current densities are 0.5 mA cm-2 (0.5 mAh cm-2) and 0.1 mA (0.1 mAh cm-2) for EO10-PFPE and EO10-CTRL composite electrolytes, respectively. (c) SEM image of the commercial Solupor separator and (d) plating/stripping performance of Na/Na symmetrical cells using composite electrolytes based on commercial Solupor separator. During long term cycling tests (after 140 h), the applied current density is set at 0.5 mA cm-2 (1.0 mAh cm-2). (e) and (f) Electrochemical impedance spectroscopy (EIS) evolution during long-term Na/Na cycling at 0.5 mA cm-2 (1.0 mAh cm-2). The cycling numbers are labeled. (g) The extracted interfacial resistance as function of cycle numbers at 0.5 mA cm-2 (1.0 mAh cm-2). The equivalent circuit is shown in the inset. Note: Figure e-g corresponds to the long-term plating/stripping test at 0.5 mA cm-2 (1.0 mAh cm-2) after 140 h as shown in Figure d. All the cell tests are performed at 80 oC

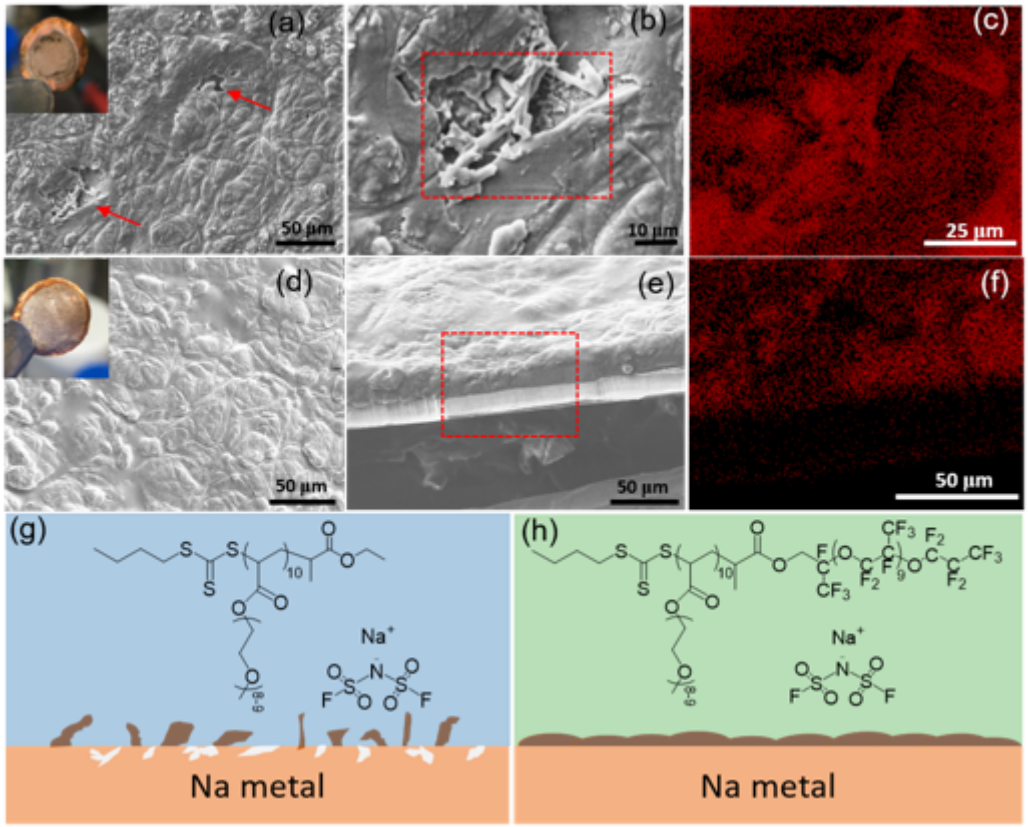

Figure 5

Morphologies of deposited Na metal. (a-b) Surface SEM images of deposited Na in a Na/Cu cell with EO10-CTRL electrolyte. (c) The corresponding Na energy dispersive spectroscopy (EDS) of the highlighted area in (b). (d) Surface SEM and (e) cross-section images of deposited Na in a Na/Cu cell with EO10-PFPE electrolyte. (f) The corresponding Na EDS of highlighted area in (e). (g-h) Schematic illustrations represent the potential SEI formation processes with different electrolytes. The inset in (a) and (d) are the digital photos of deposited Na on Cu collectors with EO10-CTRL and EO10-PFPE electrolytes, respectively. The arrows in (a) indicate dendritic deposits.

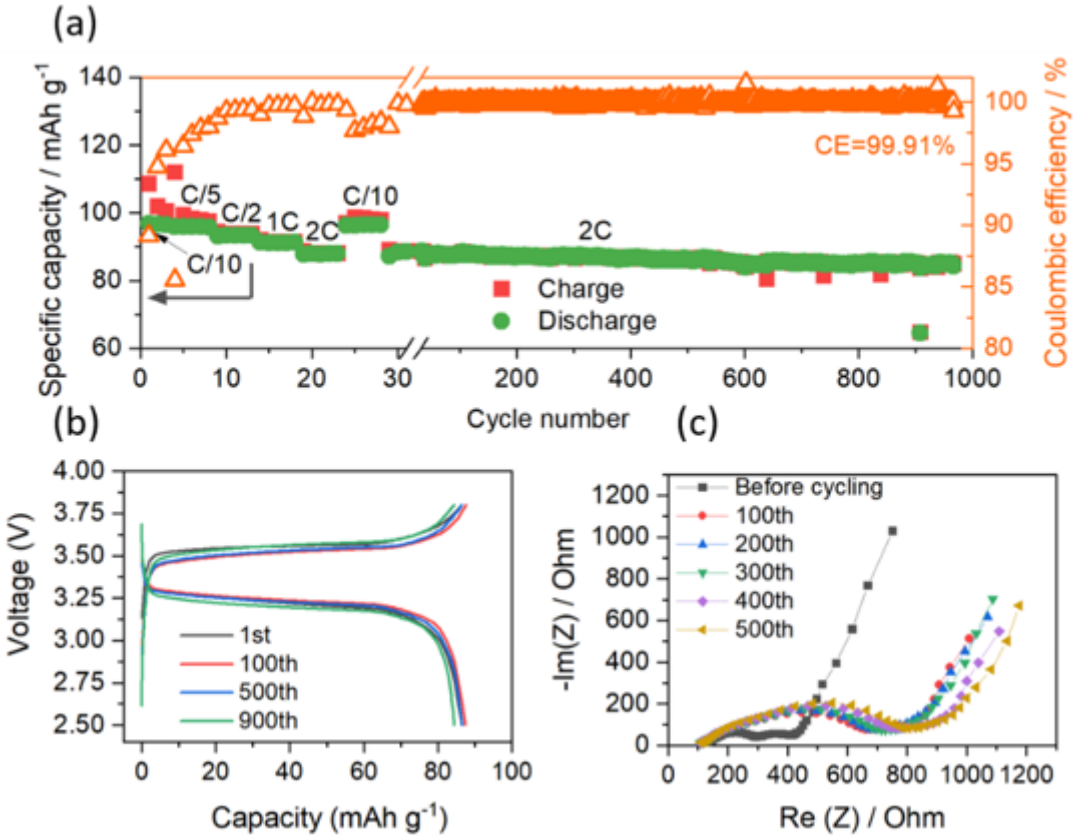

Figure 6

Electrochemical performance of Na/NVP full cells assembled with EO10-PFPE/PVDF electrolytes. (a) Charge/discharge cycling performance at various C rates and long-term stability at ≈ 0.2 mA cm-2 (2C). (b) Charge/discharge profiles of different cycles at ≈ 0.2 mA cm-2 (2C). (c) The EIS evolution during long-term cycling at ≈ 0.2 mA cm-2 (2C). The cut-off voltage is 2.5 – 3.8 V. All tests were performed at 80 oC.

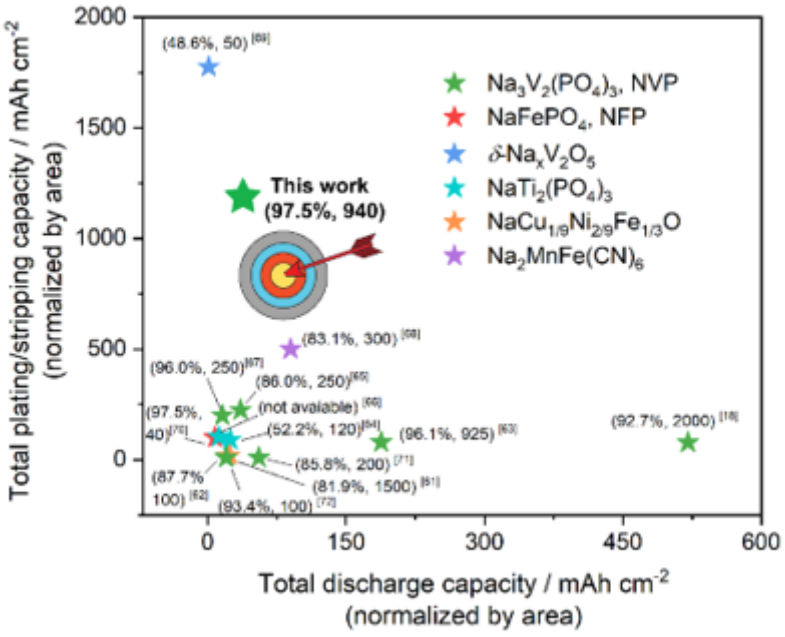

Figure 7

The comparison of total plating/stripping capacity (total charge of plated and stripped during whole Na/Na tests) and total discharge capacity (discharge capacity × cycles) based on different electrolytes and cathode materials. The capacities are normalized by area (cm2). The numbers in brackets are capacity retention and full cell cycling number, respectively. The arrow signifies the outstanding performance of PFPE-based electrolytes considering plating/stripping and full cell stability against Na metal.

Supplementary Files

This is a list of supplementary files associated with this preprint. Click to download.

- SIfinal26032021.docx